Journal of
Materials Chemistry A

Accepted Manuscript

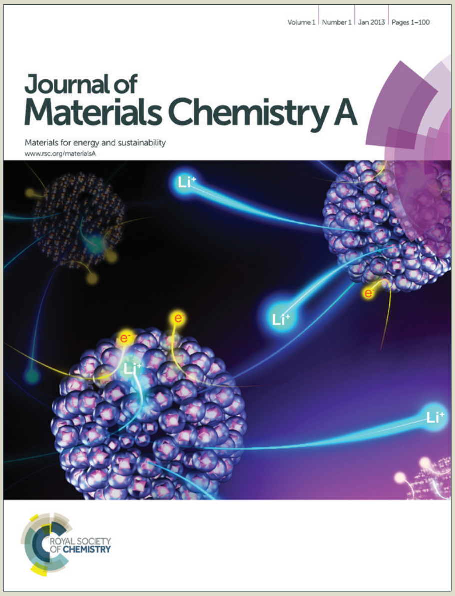

ROYAL SOCIETY
OF CHEMISTRY

www.rsc.org/materialsA

Structure and Dynamics in an organic ionic plastic crystal, *N*-ethyl-*N*-methyl pyrrolidinium bis(trifluoromethanesulfonyl) amide, mixed with a sodium salt.

Maria. Forsyth*, Tarakegn Chimdi, Aaron Seeber#, Daniel Gunzelmann and Patrick C. Howlett

Institute for Frontier Materials, Deakin University, Burwood 3125,
Melbourne, Australia

#CSIRO Process Science and Engineering, Private Bag 33, Clayton
South MDC, Victoria, Australia

*Corresponding author. mforsyth@deakin.edu.au
Tel.: +61 39902446821; fax: +61 392446868

Abstract

We present for the first time, the solid state phase behaviour of the organic ionic plastic crystal (OIPC) *N*-methyl-*N*-ethyl-pyrrolidinium bis(trifluoromethane-sulfonyl)amide, [C_2mpyr][NTf_2], upon mixing with the sodium salt, Na[NTf_2]. Whereas the behaviour of OIPCs mixed with lithium salts has been well established, the influence of adding a sodium salt has not previously been reported. The phase diagram is presented for Na[NTf_2] compositions between 1 and 50 mol%, and shows a eutectic composition at 15 mol% with a eutectic temperature at 63°C. In contrast to the lithium doping of the same OIPC, the conductivity does not increase significantly at, or below room temperature, however the material containing 40 mol% Na[NTf_2] has an ionic conductivity of 10^{-4} Scm^{-1} in the solid state at 60 ^{o}C, which is more than 3 orders of magnitude higher than the pure OIPC. Synchrotron XRD, solid-state NMR and SEM all indicate the presence of two distinct phases across all of the compositions studied. One phase is identical to that of the pure [C_2mpyr][NTf_2] and the other phase is a mixed cation compound, quite distinct from the pure Na[NTf_2] material. The higher eutectic temperature (63 °C) in the sodium based system compared to lithium (30 °C) leads to purely solid state conductivity over the entire composition range up to 63 °C.

Keywords: *N*-methyl-*N*-ethyl-pyrrolidinium bis(trifluoromethanesulfonyl)amide, solid state electrolyte, organic ionic plastic crystal, sodium, solid-state NMR, Synchrotron Powder X-ray diffraction

Introduction

Organic Ionic Plastic Crystals (OIPCs), the solid state cousins of Ionic Liquids, have been attracting attention for over a decade both from the desire to understand their intrinsic structural and dynamics characteristics [1-10] as well as for use as solid electrolytes in electrochemical devices [1, 3, 11-18] These novel materials are fully ordered, crystalline materials at low temperatures in their lowest temperature phase, and exhibit one or more solid–solid phase transitions with increasing temperature. These phase transitions result in a large entropy increase and are often associated with an order - disorder transitions. Plastic crystals maintain their long range order across all the solid phases, however, the higher temperature phases are often highly orientationally disordered and display plastic behaviour. Recently a fundamental structural and dynamic study of the Diethyl(methyl)(isobutyl)phosphonium Hexafluorophosphate (P_{1224}) PF_6 OIPC was reported [7] and clearly illustrated the complex rotational motions that were present in this archetypal plastic crystal and their relation to the phase transitions. This report also showed the power of applying a combination of complimentary characterisation methods, and in particular XRD and solid-state NMR, to elucidate the behaviour of OIPCs as will also be demonstrated in the present work.

The OIPC *N*-methyl-*N*-ethyl-pyrrolidinium bis(trifluoromethanesulfonyl) amide, $[C_2mpyr][NTf_2]$ was one of the first materials to demonstrate high ionic conductivity, in particular upon doping (or mixing) with a lithium salt. These materials have been well-studied [3, 11, 12, 16-25], with several investigations of the lithium-doped material present in the literature. In particular, Henderson et al [19] have presented a detailed phase diagram for $[C_xmpyr][NTf_2]$ salts (where x = 2-4) and have shown that several compounds potentially exist in the mixed systems, for example the 2:1 salt at 33 mol% $Li[NTf_2]$, the 1:2 salt at 66 mol% and even the 1:1 salt at 50 mol% $Li[NTf_2]$ have been suggested, although the latter is believed to be a metastable compound [19]. In these systems, perusal of the reported phase diagrams shows that the eutectic temperature is around 30°C with an apparent eutectic composition of 33 mol% $Li[NTf_2]$ in the case of $[C_2mpyr][NTf_2]$ [12, 19] and 15 mol% for the longer alkyl chains, x=3 or 4 [16, 19]. The eutectic is defined as the point in a binary phase diagram which is, by thermodynamic definition, an isothermal transition at a given composition where, upon heating, two distinct solid phases of different compositions melt to form a homogeneous liquid phase, i.e. α (solid) +β (solid) $\rightarrow$ liquid.

MacFarlane et al [11] reported that the addition of even 1 mol% Li[NTf$_2$] to the [C$_2$mpyr][NTf$_2$] OIPC increased the ionic conductivity by several orders of magnitude. Recently, Howlett et al have demonstrated the operation of lithium metal cells based on [C$_2$mpyr][NTf$_2$]/Li[NTf$_2$ [17, 18] as well as [C$_2$mpyr]BF$_4$/LiBF$_4$ [26] solid electrolytes. The mechanism of conductivity enhancement in these materials is still under debate. It has been shown that, the addition of Li salts to OIPC creates more vacancies [23, 27, 28] and this is suggested to lead to a higher concentration of more diffusive ions, thus higher conductivity. On the other hand, an alternative conduction mechanism has been suggested recently, whereby the high ionic conductivities are a result of an interconnected, percolating pathway of a metastable liquid phase, rich in lithium ions [16] rather than solid state diffusion of lithium ions. A similar mechanism has also recently been proposed for an acid ‘doped’ organic crystal Guanidinium Triflate [29] and high proton conductivity due to the presence of a liquid phase has also been suggested for a H$_3$PO$_4$ containing choline dihydrogen phosphate OIPC [30].

Fast ion sodium conductors have been known for some time in the ceramics field with the beta-alumina material being one of the best known Na$^+$ conductors [31, 32] and is currently the solid state electrolyte in the Na Zebra battery [33]. This battery operates above 300°C primarily due to the fact that the Na$^+$ conductivity is insignificant below this temperature. Fast ion Na$^+$ conduction in plastic crystalline materials has also been reported at high temperatures in the inorganic plastic crystalline phases found in Na$_3$PO$_4$ and Na$_2$SO$_4$ [34-36]. Until now, the effect of adding sodium ions to an OIPC has not been considered. If the Na$^+$ transport behaviour is similar to lithium based systems, then these materials may be useful in the development of lower temperature solid state Na devices. In this work we have investigated the effect of adding Na[NTf$_2$] to [C$_2$mpyr][NTf$_2$] on the phase behaviour and conductivity using DSC, Synchrotron XRD, vibrational spectroscopy and VT multinuclear solid-state NMR spectroscopy.

Experimental

Material preparation

Highly purified ionic plastic crystal *N*-methyl-*N*-ethyl-pyrrolidinium bis (trifluoromethanesulfonyl) amide ($[C_2mpyr][NTf_2]$) was purchased from Solvionic, sodium bis(trifluoromethanesulfonyl)amide ($Na[NTf_2]$) salts were purchased from Sigma Aldrich Inc. Due to the hygroscopic nature of the samples, all materials handling was performed under a high purity argon environment in a glove box. Pure amounts of $[C_2mpyr][NTf_2]$ and $Na[NTf_2]$ were mixed together and heated into the melt. Thereafter, the samples were allowed to completely dissolve for 4 hours at 90°C using a stirring centrifuge running at 300 rpm. Samples were dried at 110 °C under vacuum for 15 h, and stored in a glove box under an Argon environment. Compositions of 1, 2, 4, 6, 8, 10, 15 30, 35, 40 and 50 mol% of $Na[NTf_2]$ were prepared.

Differential Scanning Calorimetry (DSC)

A Mettler Toledo differential scanning calorimeter (DSC) - DSC822^e was used to investigate the thermal properties of the samples. Vacuum dried powder samples of less than 10 mg were loaded into DSC crucibles in the Argon glove box and sealed. STAR^e V6.10 software was used for instrument control and data analysis. Thermal properties of the samples (both pure and mixtures with $Na[NTf_2]$) were recorded over a temperature range of −150 to 150 °C with a scanning rate of 10 °C min^{-1}.

Electrochemical Impedance Spectroscopy

Impedance spectra were obtained using a BioLogic SP-200 potentiostat equipped with EC-Lab V10-12 software. Pellets in the range of thickness of 0.5–0.8 mm and a diameter of about 13 mm were prepared by pressing in a KBr die under 7 tons of load for 5 minutes. The prepared pellets were sandwiched between two circular stainless steel electrodes in hermitically sealed conductivity cells (Advanced Industrial Services, Moorabbin, Australia). Data were collected over a frequency range of 50 mHz – 7 MHz in a temperature range from 25 – 80 °C at 5 °C intervals under single sine wave acquisition mode at 200 mV signal voltage amplitude and auto current mode. The temperature was controlled using a Eurotherm model 3504 temperature controller and a 28V/32W heater (Helios Electroheat Pty Ltd, Cheltenham, Australia). An equilibration time of 45 min was used to stabilize the temperature at −30 °C before the beginning of the measurement. An interval of 30 min was allotted between each measurement temperature (i.e., after each 5 or 10 °C step). Multiple measurements were carried out to check for stability and reproducibility in the Nyquist plots for each of the samples. The Nyquist plots of the impedance data were used to determine the sample resistance from the intercept (or the first touch-down) of the real axis.

Scanning Electron Microscopy (SEM)

Scanning Electron Microscopy (SEM) was used to study topography and morphology of the samples. A high resolution JCM -5000 Neoscope (Jeol Ltd.) at 5 kV was used to record the micrographs. Powder samples were prepared in a glove box and put on carbon tape and then flushed with N_2 to avoid dispersing of the powder into the equipment.

Raman / IR spectroscopy

Raman measurements were conducted using a Renishaw InVia Raman Microspectrometer (Renishaw plc, Gloucestershire, UK), equipped with a 633 nm HeNe laser (RL633 HeNe, Renishaw plc, Gloucestershire, UK) and a thermo-electrical cooled CCD detector. Acquisition parameters used for spectral data collection included a 10 s exposure time and 4 cm^{-1} spectral resolution. Spectral analysis was performed using WiRE 3.4 (Renishaw) software.

ATR-FTIR spectral data was acquired on an Alpha FTIR spectrometer (Bruker Optik GmbH, Ettlingen, Germany) equipped with a deuterated triglycine sulfate (DTGS) detector. The spectrum was collected on a clean surface of ATR diamond crystal by pressing few milligrams of the samples using a metal clamp. OPUS 7.0 software suite (Bruker) was used to record the ATR-FTIR measurements with the acquisition parameters of 4 cm^{-1} spectral resolution, 64 co-added scans, Blackman-Harris 3-Term apodization, Power-Spectrum phase correction, and zero-filling factor of 2

Synchrotron X-ray Powder Diffraction (XRD)

Variable temperature Synchrotron X-ray Powder Diffraction (XRD) on pure $[C_2mpyr][NTf_2]$ and 15 mol% $Na[NTf_2]/[C_2mpyr][NTf_2]$ was conducted at the Australian Synchrotron, Powder Diffraction Beamline. The beamline uses an array of 16 MYTHEN 1D microstrip silicon detectors with each module spanning about 5 degrees in 2θ to enable collection of data covering over 83°. The single-photon counting mode and high dynamic range of the beamline provide an excellent signal-to-noise at the photon energy of 12.4 keV and current of ~200 mA. The powder samples were sealed in 0.3 mm borosilicate glass capillaries (Charles Supper Company, Massachusetts, USA) within an argon atmosphere glove box. Prior to data collection, the wavelength was set at 1.00025 Å using a Si111 double crystal monochromator and calibrations were made with NIST reference material LaB_6. A Cyberstar hot-air blower was used to control the temperature within 0.1-0.2 °C for all data collection temperatures. Data were recorded for 5 min at each of the two detector settings after the control sensor had reached the set point temperature and equilibrated for 3 min.

Solid State Nuclear Magnetic Resonance Spectroscopy

All samples were studied using commercial Bruker AVANCE III 300WB and 500WB NMR spectrometers equipped with Bruker double- and triple-resonance magic-angle-spinning (MAS) solid-state NMR probes. The powder samples were packed in 2.5 and 4 mm ZrO_2 MAS rotors in an argon glove box. ^1H, ^{19}F, ^{13}C and ^{23}Na NMR experiments were performed at Larmor frequencies of 500.13, 470.59, 75.49 and 79.39 MHz, respectively, using a magic-angle-spinning frequency of 27.5 kHz for proton and fluorine, and 12.5 kHz for carbon and sodium measurements at ambient temperature. All proton and carbon spectra were referenced externally relative to TMS, all fluorine shifts are given with respect to $CFCl_3$ and the sodium shifts relative to a 1 M NaCl solution.

For the ^1H and ^{23}Na NMR experiments a solid-echo pulse sequence ($90 - \tau - 90 - \tau -$ acq) was used, for ^{19}F the antiring [37] pulse sequence with recycle delays of 0.4-10s were used applying excitation rf pulses with nutation frequencies of 139 kHz, 125 kHz and 96 kHz for ^1H, ^{19}F and ^{23}Na, respectively. Recycle delays were set to at least 3-5 times the T_1 value, which were measured prior via the Saturation Recovery method, to ensure a complete recovery of magnetisation. ^{13}C spectra were recorded using cross-polarization (CP) from proton to carbon to enhance the signal/noise ratio. CP contact times of 3–4 ms and recycle delay times of 2–3 s were used. Simultaneous broadband ^1H and ^{19}F decoupling was applied during carbon acquisition via the SPINAL64 [38] sequence for protons and a rotor-synchronous Pi decoupling for fluorine using a decoupling field strength of 100 kHz on both channels. The VT MAS experiments were conducted with a 2.5 mm MAS probe operating at 500.13, 470.59 and 132.28 MHz for ^1H, ^{19}F and ^{23}Na, respectively, in a temperature range of 253 – 348 K. Real sample temperatures for a nominal set temperature and MAS rate were corrected according to a temperature calibration applying the general protocol proposed by Stark [39] using a ~ 2:1 mixture of $Pb(NO_3)_2$ and NaF as chemical-shift thermometer [40] as well as ^{19}F and ^{23}Na shift reference. The experimental deviation of the real sample temperatures from the corrected, set values is estimated at less than 0.5 K for 0 - 30°C, but up to ± 3 K for temperatures over 40°C. Further details are given in the figure captions.

Results and Discussion

Thermal analysis

Figure 1 presents the thermograms for pure $[C_2mpyr][NTf_2]$ and the binary mixtures with $Na[NTf_2]$ at different concentrations. No evidence of a glass transition was observed in the investigated temperature range. The melting temperatures of pure $[C_2mpyr][NTf_2]$ and $Na[NTf_2]$ were 91 ^oC and 257 ^oC, respectively, and are consistent with prior reports [11, 12].

As several previous studies have shown, $[C_2mpyr][NTf_2]$ undergoes several solid-solid phase transitions [5, 11, 22, 25, 41] and the data here are in agreement with previous measurements of this material. Thus, the transition from ordered phase IV to disordered phase III was observed at -85 ± 1^oC followed by the phase III to phase II transition occurring at 17 ± 1^oC. The phase transition before the melting point of $[C_2mpyr][NTf_2]$ at 91 ± 1^oC, occurred at 45 ± 1^oC and is assigned to solid-solid transition from disordered phase II to disordered phase I. Figure 1 also shows that, the solid-solid transitions from phases IV-III, III-II and II-I (dashed lines) of the binary systems are consistent with the pure materials and no peak shift with respect to the pure OIPC was observed. For the binary systems containing $Na[NTf_2]$, an extra peak is observed at 63 ± 2^oC and this peak increases in enthalpy relative to the final melting peak. As is typical of a mixed system, the melting peak transition shifts to lower temperatures and broadens significantly. At 15 mol% only the sharp peak at 63°C is observed. Given the behaviour of this transition, we assign it to the eutectic temperature, T_E, with 15 mol% being the eutectic composition. Thus, at this composition, above T_E the material is completely liquid whereas below this temperature the material solidifies into two distinct phases (denoted α and β). We will discuss this in more detail following the presentation of the XRD and NMR data. For other binary compositions, the materials begin to melt at T_E but two phases (a liquid phase and a solid phase) co-exist until the final melting point (also known as a liquidus temperature). The DSC traces for the compositions greater than 15 mol% Na^+ shown in figure 1, display the eutectic transition, T_E, and a further melting peak consistent with a new solid phase, labelled β in the binary phase diagram shown in figure 2.

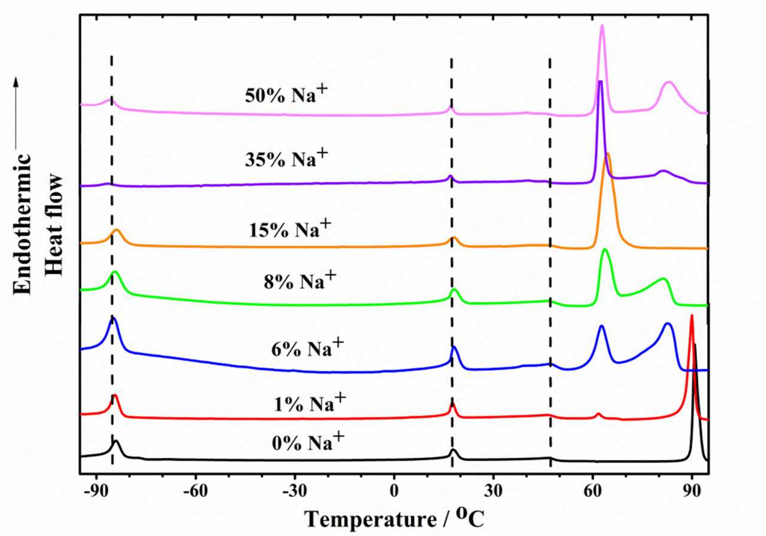

Figure 1. DSC traces of pure $C_2mpyr[NTf_2]$ and mixtures (1-50 mol%) of $Na[NTf_2]$ with $[C_2mpyr][NTf_2]$.

The partial binary phase diagram presented in Figure 2 more clearly shows the phase behaviour of the $Na[NTf_2]/[C_2mpyr][NTf_2]$ system. It can be observed that the melting point is decreased and the eutectic transition occurs at 63 ± 2 °C at 15 mol% $Na[NTf_2]$ content. The solid-solid phase transitions are still evident at all studied Na^+ contents and indicate that one of the solid phases is very similar to the pure $[C_2mpyr][NTf_2]$. Table S1 presents the enthalpy of transitions for each system. The enthalpy of the melting transition associated with the pure OIPC phase decreases with increasing Na^+ concentration with a concomitant increase in the enthalpy of the eutectic transition until 15 mol%, beyond this concentration, the eutectic transition decreases in enthalpy whilst a new melting transition (liquidus) associated with a second solid (β) phase appears. This phase diagram is very similar in appearance to the [$C_x$mpyr][NTf_2]/Li[NTf_2] binaries [19]. The eutectic composition of about 15 mol% was observed from [C_3mpyr] and [C_4mpyr], however T_E was approximately 30 °C when Li[NTf_2] was mixed into the [C_2mpyr][NTf_2] OIPC [19].

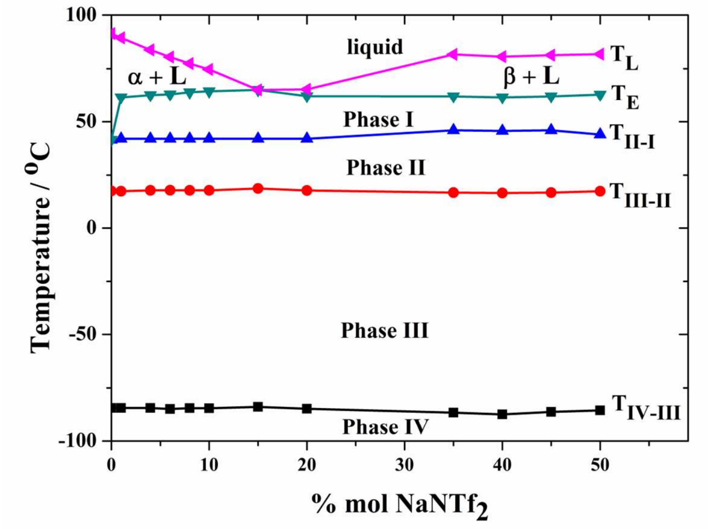

Figure 2. Phase diagram for [C_2mpyr][NTf_2]/Na[NTf_2] shows solid-solid phase transition temperatures T_{IV-III}, T_{III-II}, T_{II-I}, eutectic temperature T_E and liquidus temperature T_L.

Morphology

Figure 3 presents SEM images of the binary materials for 2 mol% Na[NTf_2], 1mol% Li[NTf_2] and pure C_2mpyr[NTf_2]. The images demonstrate the periodic slip planes previously observed in the pure OIPC [42]. In contrast to 1 mol% Li[NTf_2], the grain boundaries in the Na[NTf_2] containing sample do not appear to have coarsened and instead, small particles can be seen dispersed throughout the matrix in Fig 3d. Given the phase diagram shown in figure 2, these particles could be the second, Na^+ rich β phase, which would be the minority phase at this composition.

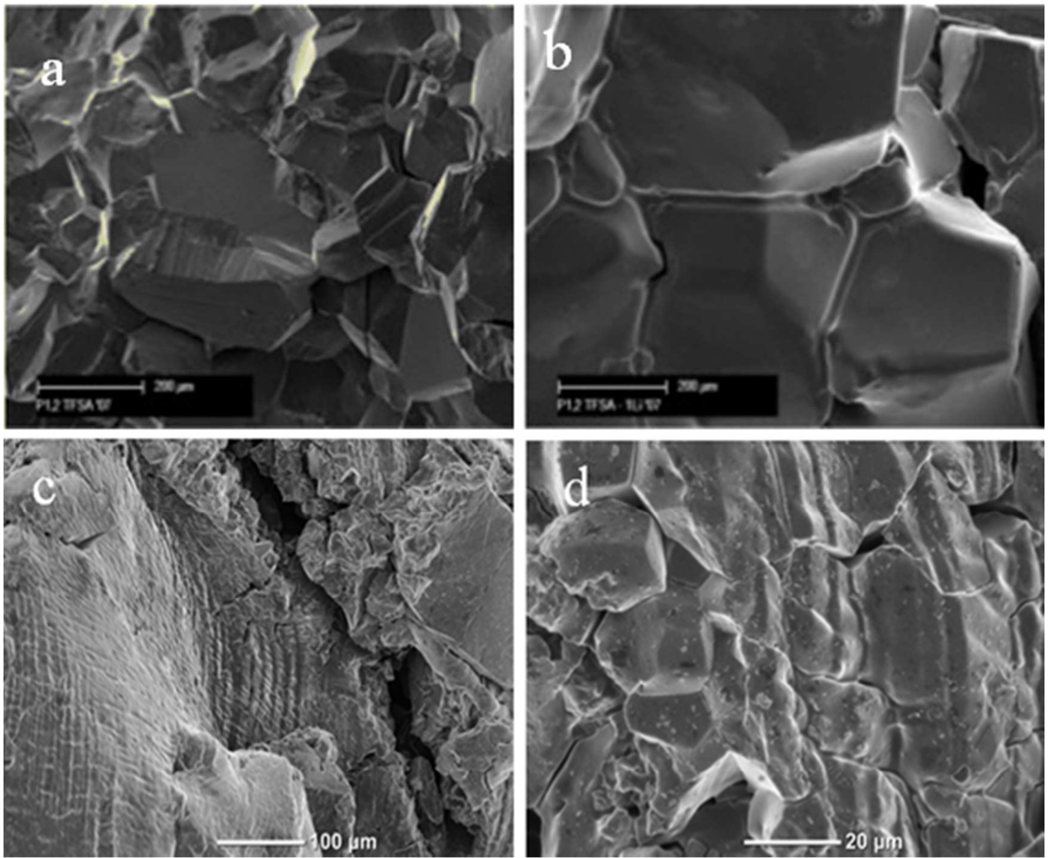

Figure 3. Micrographs showing a comparison of [C_2mpyr][NTf_2] OIPC a) pure 200 µm scale bar [42]; b) mixed with 1% mol Li [NTf_2], 200 µm scale bar ; c) mixed with 2% mol Na[NTf_2], 100 µm scale bar and d) mixed with 2% mol Na[NTf_2], 20 µm scale bar.

Conductivity behaviour in the Na[NTf_2]/[C2mpyr][NTf_2] binary system compared with the Li[NTf_2]/[C2mpyr][NTf_2] binary system

The conductivity of [C_2mpyr][NTf_2] and mixed Na[NTf_2] systems are shown in Figure 4 as a function of temperature for the compositions with 0, 4, 15 and 40 mol% Na[NTf_2]. In contrast to the behaviour upon addition of Li[NTf_2], shown as inset in Figure 4, it can be seen that the conductivity of the mixed systems is lower than the pure OIPC below the onset temperatures of the phase II–I solid-solid transition for all compositions. Beyond the Phase II–I transition there is a significant increase in conductivity compared to the pure sample, approximately one order of magnitude for the 15 and 40 mol% Na[NTf_2] samples at 50 °C. The conductivity further increased by three orders of magnitude to over ~3 x 10^{-4} S/cm in the case of 40 mol% Na[NTf_2] at 60 ^{o}C, just below the eutectic melt. According to the phase diagram this composition should still be completely solid at this temperature.

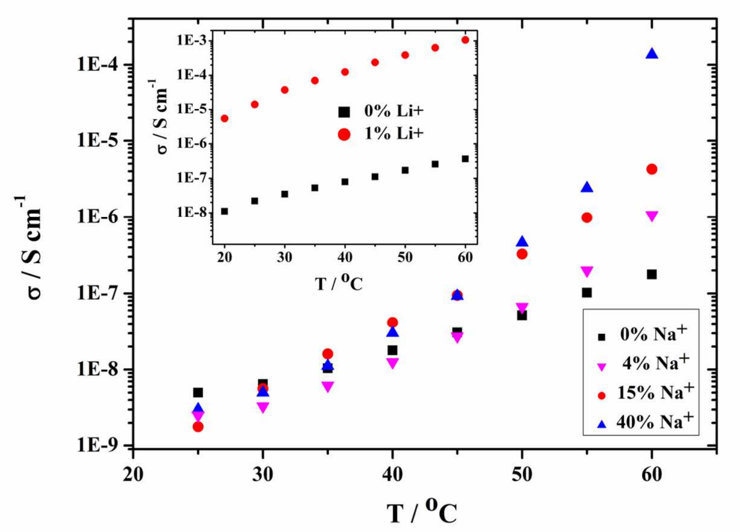

Figure 4. Ionic conductivity of pure and Na^+ mixed [C_2mpyr][NTf_2] with variable Na[NTf_2] concentration. (The ionic conductivity of pure and 1 mol % Li^+ mixed [C_2mpyr][NTf_2] is compared in the *inset* [43]).

This is in contrast with the Li[NTf_2] mixtures where the eutectic temperature occurred at 30 °C, and therefore, above this temperature there would likely be a Li^+ rich, liquid phase present in the material. This could account in part for the high conductivities observed in those systems even at lower temperatures and compositions [11, 12, 23, 25]. Furthermore, whereas the lithium additions appeared to lead to coarser grain boundaries, the Na[NTf_2] addition instead leads to a dispersed second phase that does not appear to contribute the conduction processes at lower temperatures (i.e, phases IV-II, below 45 °C), as can be inferred from the similarity of the measured conductivity values at these temperatures.

The eutectic temperature for these systems was consistently 62 °C to 65 °C (as observed on the phase diagram Figure 2) and would suggest an uncertainty in the measurement of about +/- 1.5 °C. At the eutectic composition (15 mol%) the entire sample ‘melts’ at the eutectic temperature whereas for all other samples there will be some liquid and residual solid with the amount of liquid increasing till the final melt. This would mean that if the conductivity of any of the samples was influenced to any extent by the presence of a liquid phase this would be the 15 mol% eutectic composition rather than the 40 mol% sample, which is clearly not the case.

Synchrotron X-ray diffraction (SXRD)

The X-ray powder diffraction patterns for [C$_2$mpyr][NTf$_2$] plastic crystal and the mixed system containing 15 mol% Na[NTf$_2$] (Na$_{0.15}$[C$_2$mpyr]$_{0.85}$[NTf$_2$])_ were measured at the Australian Synchrotron at temperatures of 273, 303 and 328K, which correspond to phases III, II and I respectively and are presented in Figure 5. These phases are different from those in previous reported work [24] at 153K (phase IV), and the phases at 213K (phase III) [24] and 273K (phase III) in the current work are both triclinic.

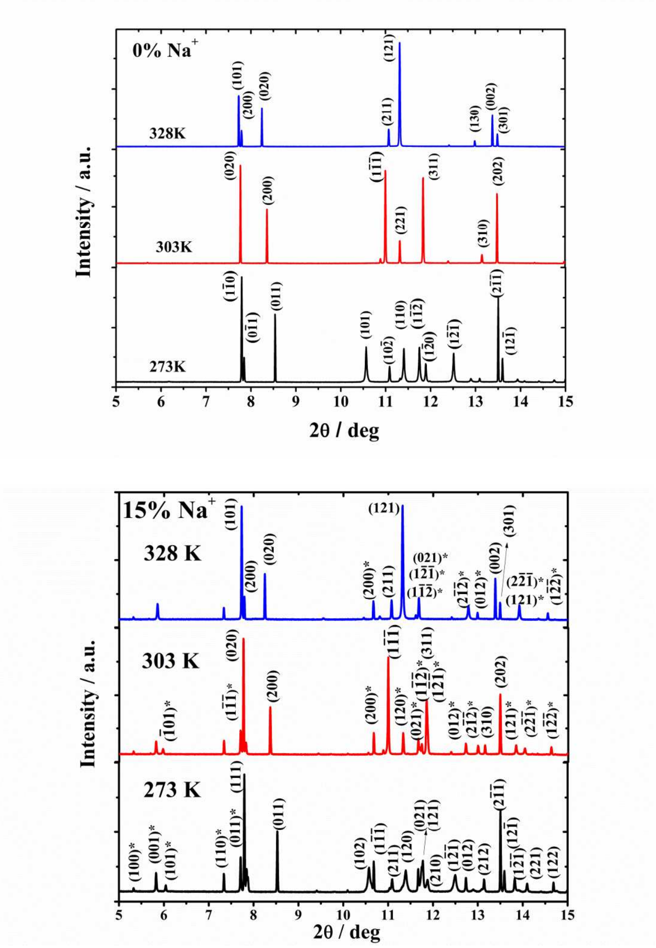

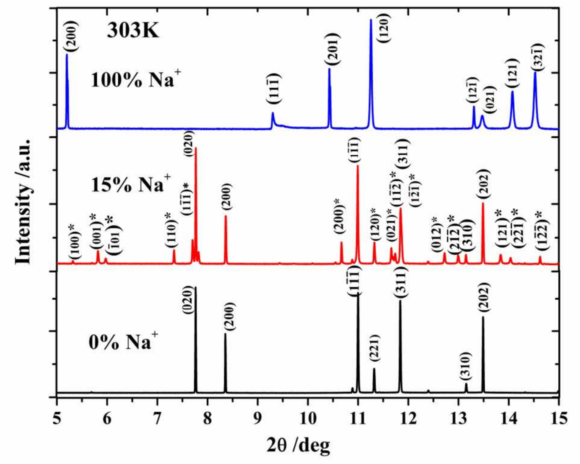

Figure 5. Indexed synchrotron XRD patterns acquired for (a) [C$_2$mpyr][NTf$_2$] and (b) Na$_{0.15}$[C$_2$mpyr]$_{0.85}$[NTf$_2$] at temperatures of 273, 303 and 328K (i.e., phases III, II and I respectively). A comparison of pure OIPC and NaNTf$_2$ components and Na$_{0.15}$[C$_2$mpyr]$_{0.85}$[NTf$_2$] at 303K is shown in (c).

To investigate the phase changes of the pure and mixed systems at a series of temperatures, a total pattern of synchrotron X-ray data was analyzed using the TOPAS Academic v4.2 Coelho software [44]. On indexing the reflections from the synchrotron X-ray data, it was found that the pure OIPC undergoes several phase changes with increasing temperature. The lattice parameters and space groups for the major OIPC phase are presented in Table 3a. The same lattice parameters, characteristic of the [C$_2$mpyr][NTf$_2$] phase, were also retained in the Na$_{0.15}$[C$_2$mpyr]$_{0.85}$[NTf$_2$] system while the second phase (Table 1b) was indexed from the peaks remaining.

Table 1a: Lattice parameters determined for [C$_2$mpyr][NTf$_2$] OIPC.

Crystal system	Triclinic	Monoclinic	Orthorhombic
Space group	P-1	CC	I222
a /Å	8.5668	15.5696	14.7159
b /Å	10.0054	14.7694	13.9056
c / Å	11.1919	8.5554	8.5865
α /deg	88.0068	90	90
β /deg	107.624	61.779	90
γ /deg	111.200	90	90
V /Å^3	849.391	1733.492	1757.066
ρ /g/cm^3	1.542	1.511	1.490
Z	2	4	4
2θ$_{max}$ /deg	83	83	83

Table 1b: Lattice parameters determined for the mixed phase in $Na_{0.15}[C_2mpyr]_{0.85}[NTf_2]$ OIPC.

Crystal system	Triclinic	Monoclinic	Orthorhombic
Space group	P-1	CC	I222
a /Å	8.5668	15.5696	14.7159
b /Å	10.0054	14.7694	13.9056
c / Å	11.1919	8.5554	8.5865
α /deg	88.0068	90	90
β /deg	107.624	61.779	90
γ /deg	111.200	90	90
V /Å^3	849.391	1733.492	1757.066
ρ /g/cm^3	1.542	1.511	1.490
Z	2	4	4
$2\theta_{max}$ /deg	83	83	83

As shown in Table 1a, the lattice parameters of the pure OIPC undergo crystal structure changes at temperatures of 273, 303 and 328K as evidenced in the XRD patterns shown in Figure 5. The synchrotron powder XRD data for the pure OIPC suggests that phase III (273K) is triclinic P-1, while phases II (303K) and I (328K) are monoclinic CC and monoclinic C2, respectively. The lattice parameters for the phase III structure (273K) agree well with the previous study [24] at 213K, with a slight increase in volume/decrease in density which is expected from thermal disorder responsible for the rotational disorder in both the $[C_2mpyr]^+$ cation and the $[NTf_2]^-$ anion. The increase in volume can be seen in the XRD traces through peak shifts to lower 2θ values. At 303K, in phase II, the XRD trace is characterised by a general shift of diffraction peaks to lower 2θ values, and the disappearance of Bragg peaks is consistent with the change in the crystal structure to high symmetry monoclinic C2. A slight increase in volume was observed in the second (β) phase (different from $NaNTf_2$) as shown in Table 3b. Contrary to the OIPC rich phase, there is no change in the space group for the mixed phase at these temperatures; only an elongation of the crystallographic axes. These findings are consistent with the binary phase diagram and SEM micrographs shown above; As shown in Figure 2, the binary systems do not allow for significant solid solutions (<1%) and phase transitions are either for the OIPC or a second Na rich phase.

Figure 5a presents a comparison of the data for the pure OIPC at each of these temperatures, Figure 5b compares the XRD patterns for the 15 mol% Na[NTf$_2$] sample at each temperature, and Figure 5c compares the XRD pattern at 303K for the two pure components [C$_2$mpyr][NTf$_2$], Na[NTf$_2$] and the Na$_{0.15}$[C$_2$mpyr]$_{0.85}$[NTf$_2$] mixture. The measurement at 303K was reproduced upon both heating and cooling the samples. In the both pure OIPC and Na$_{0.15}$[C$_2$mpyr]$_{0.85}$[NTf$_2$] materials, as the temperature is increased, the diffraction peaks shift towards the lower 2θ, split peaks appear to merge and many of the weaker peaks disappear. The shift to lower 2θ values are consistent with an expansion of the lattice parameters and the disappearance of peaks at higher temperatures is attributed to changes in the crystalline phases and/or crystal symmetry. Peak broadening was also observed in these Na$^+$ mixture materials, contrary to the pure OIPC at 273K.

The XRD patterns for the mixture shown in Figure 5b were significantly more complex than for the pure OIPC. Although the same behaviour in terms of shifts in 2θ and the loss of weaker peaks is evident in this mixture, the numerous additional peaks gives a strong indication for the presence of a new second phase. A comparison of the traces for the pure Na[NTf$_2$] (Figure 5c) salt shows that these extra diffraction peaks are not simply insoluble Na[NTf$_2$] but rather a new compound that incorporates both cations.

From previous studies on the OIPCs it had been known that defects [23, 45] play a vital role in the transport processes. Meanwhile, these materials also undergo plastic deformation due to extended defects in their high temperature phases and have complex microstructures containing grains, sub-grains, dislocation cells, as has been shown in the SEM micrographs. These microstructural complexities result in crystallite and grain sizes variations. In previous XRD studies [46] on different materials it had been suggested that shifts in Bragg peaks as well as broadening of the peaks can be caused by internal stresses, stacking faults, twin boundaries, grain boundaries and chemical heterogeneities. Thus some of the changes observed between the pure OIPC and the mixed system for the OIPC related peaks can be associated with these defects.

NMR Spectroscopy

Solid-state NMR was used to study the structural and dynamic behavior of the samples in relation to the Na^+ ion content. The composition of the OIPC allows each component (i.e., Na^+, $[C_2mpyr]^+$ and $[NTf_2]^-$) to be specifically probed due to the presence of unique NMR active nuclei. Thus, ^1H NMR is used to study the $[C_2mpyr]^+$ cation, ^{19}F for the $[NTf_2]^-$ anion, and ^{23}Na for the added Na^+ ions. ^{13}C and ^{15}N CPMAS spectra were used to study the local environment of both OIPC ions, however ^{15}N NMR spectra only gave weak signals at very long experiment times and thus were not performed on all samples.

The proton NMR spectra of the samples with varying Na^+ content do not show a significant change in the Na^+ substituted materials (see Figure 6a). All peaks can be assigned to the $[C_2mpyr]^+$ as given in [47]. The quite narrow lines in the proton spectra indicate the high rotational disorder of the molecule which averages the dipolar interactions present in solids and thus decreases the line width in the proton solid-state spectra.

In the ^{19}F spectra however, several significant changes were observed (see Figure 6b). The spectrum of the $Na[NTf_2]$ shows two different peaks, indicating unequal environments, which we assign to two conformations of the dihedral angle to the CF_3 groups in the anion $[NTf_2]$. The pure $[C_2mpyr][NTf_2]$ spectrum however gives one single signal. This means the CF_3 groups are in the same environment and move fast enough to average out any conformational or crystallographic differences. For the samples with different sodium contents a series of spectra were recorded which display a continuous transition between the two neat materials with additional signals of increasing intensity for increasing Na^+ content (within the studied concentration range). These are assigned to the second phase, in agreement with SXRD measurements, and indicate a different structure of the amide anion in the second phase relative to the structures of the pure components.

Another significant change can be observed in the ^{13}C CPMAS spectra (see Figure 6c). Here both, cation and anion, are probed together and show additional signals with increasing Na^+ content. The neat $Na[NTf_2]$ spectrum shows just one signal for the CF_3 groups of the $[NTf_2]^-$, the neat $[C_2mpyr][NTf_2]$ spectrum shows the assigned signals [47] of both the cation and anion. With the addition of Na^+ to the system, additional peaks can be observed in roughly the ratio of Na^+ substitution in the second, Na rich phase (taking unreliable integration of CPMAS spectra into account and assuming that all of the Na^+ ions are in this second phase). This confirms the SXRD evidence for a second phase where the additional signals can be interpreted as arising from cation and anion components of the additional phase which has a structure different to Na[NTf_2] and [C_2mpyr][NTf_2].

A similar behavior can be observed in the ^{23}Na spectra (see Figure 6d). The pure Na[NTf_2] shows a typical quadrupolar line shape with a chemical shift δ_{iso} of -11.7 ppm, a quadrupolar coupling C_Q of 1.114 MHz and an asymmetry parameter η_Q of 0.5, whereas the binary mixtures show a line shape with δ_{iso} -10.5 ppm, a C_Q of 1.621 MHz and an asymmetry parameter η_Q of 1.0 . This indicates that Na^+ ions in the mixtures occupy a different crystallographic environment than in the neat material. The inability to observe the additional phase in the ^{23}Na spectra could either be caused by the low sodium contents in the [C_2mpyr][NTf_2] rich phase, which make it very demanding to get enough signal intensity or alternatively the Na ions are in a very similar environment which would result in a very similar line shape and shift thus becoming indistinguishable from the Na[NTf_2] rich sample. Further studies on the structure and conformation of the additional phase are ongoing.

Variable temperature MAS NMR (VT-MAS) was performed on all materials to study the phase behavior of the cations and the anion using ^{1}H, ^{23}Na and ^{19}F nuclei as site selective probes. The temperature region studied covers phases III to I (and for 15 mol% Na^+ also extends into the liquid phase). For the ^{1}H nuclei shown in Figure 7, the broad peaks observed below 295 K undergo a significant line narrowing at higher temperatures (i.e., at 323K in phase I and at 349K above the eutectic temperature) to a typical two phase spectrum with a liquid-like mobile component and a smaller, broad linewidth spectrum of a less mobile solid component.

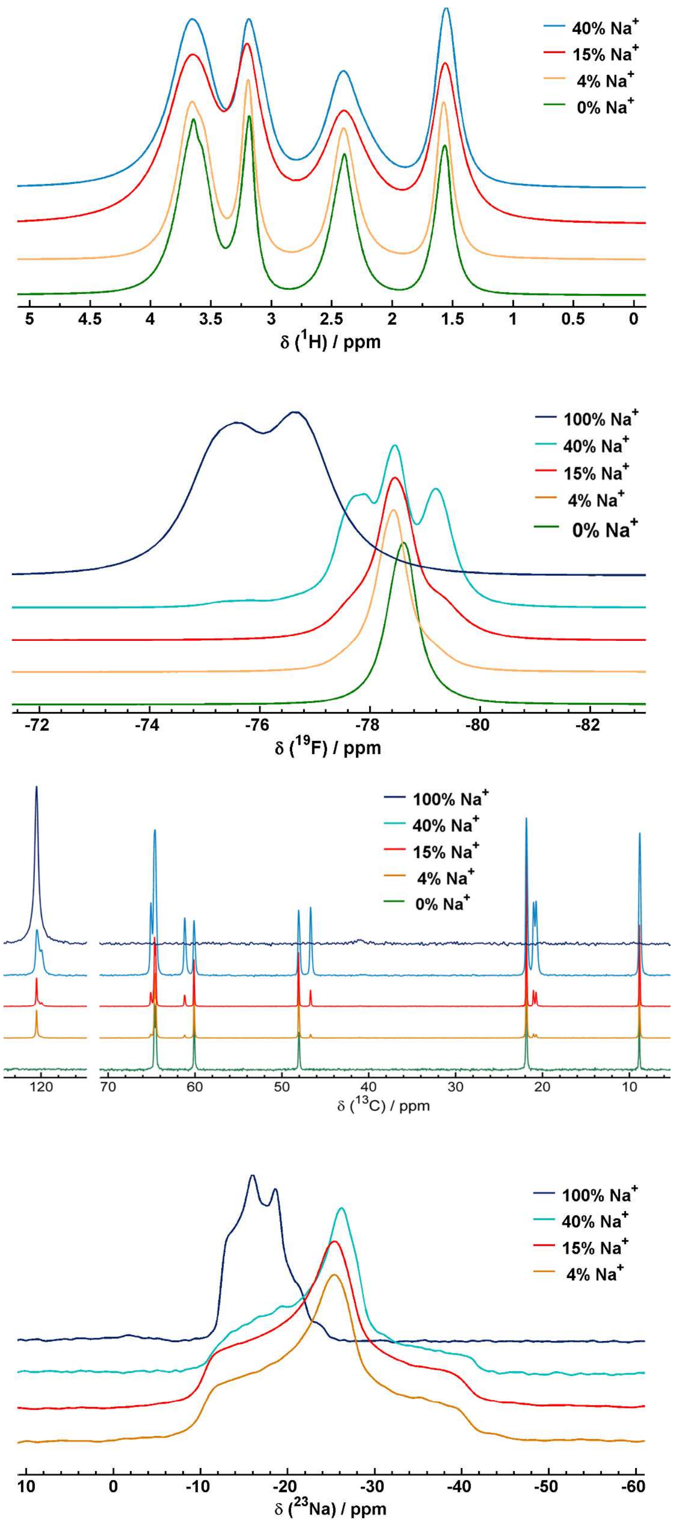

Figure 6. ^{1}H, ^{19}F, ^{13}C, and ^{23}Na MAS solid-state NMR spectra (a–d respectively) at ambient temperature (295K) for the binary mixtures from 0 to 100 mol% Na^{+} content.

This correlates well with the phase behavior in the ‘α + L’ region (where α represents the OIPC rich phase). At a temperature of 349 K a spectrum of the $Na_{0.15}[C_2mpyr]_{0.85}[NTf_2]$ melt with narrow signals is measured (see Figure 7b). The anions were investigated via the ^{19}F nuclei within the same temperature range and showed similar trends as the ^1H spectra (Figure 8). The broadened signals at lower temperatures narrow slightly, up to the eutectic temperature, then exhibit the two phase spectrum of the ‘α + L’ region and very narrow signals above the melting temperature. The ^{23}Na VT-MAS spectra (Figure 9) show the quadrupolar line shape, but no significant line narrowing or change in the line shape or chemical shift could be observed for the phase I or II temperature region. For the melt however, the spectra change significantly to a gaussian broadened isotropic line at δ = -10 ppm. This correlates well with highly mobile Na^+ ions in an ionic liquid.

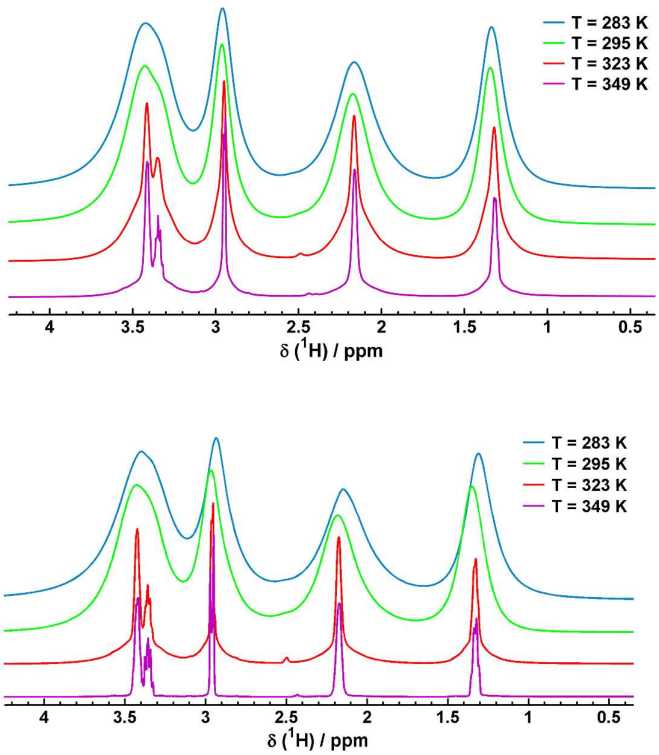

Figure 7. ^1H VT-MAS solid-state NMR spectra for the binary mixtures a) $Na_{0.04}[C_2mpyr]_{0.96}[NTf_2]$ and b) $Na_{0.15}[C_2mpyr]_{0.85}[NTf_2]$ acquired between 283K and 349K.

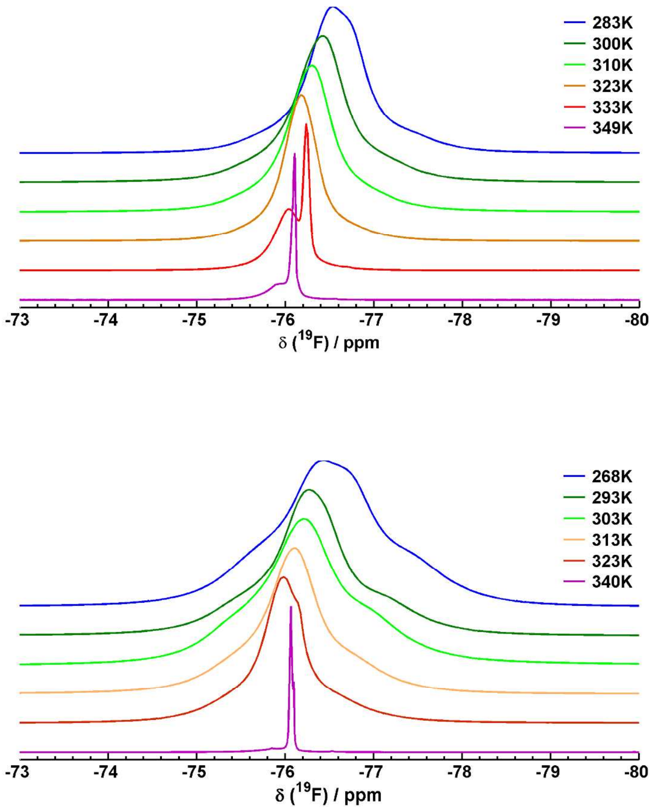

Figure 8. ^{19}F VT-MAS solid-state NMR spectra for the binary mixtures a) $Na_{0.04}[C_2mpyr]_{0.96}[NTf_2]$ and b) $Na_{0.15}[C_2mpyr]_{0.85}[NTf_2]$ acquired between 268K and 349K.

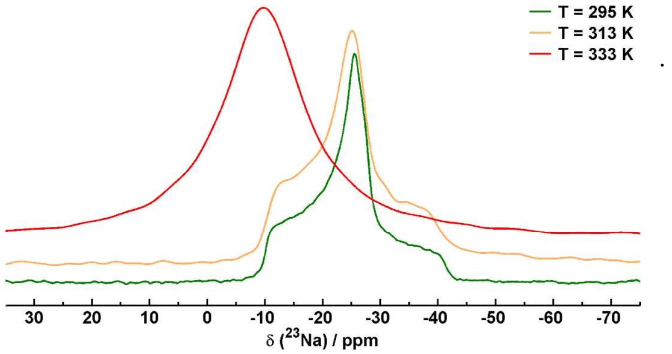

Figure 9. ^{23}Na VT-MAS solid-state NMR spectra for $Na_{0.15}[C_2mpyr]_{0.85}[NTf_2]$ acquired at 295K, 313K and 349K

IR/Raman spectroscopy

Room temperature FTIR and Raman spectra were acquired for $[C_2mpyr][NTf_2]$, $Na[NTf_2]$, $Na_{0.04}[C_2mpyr]_{0.96}[NTf_2]$ and $Na_{0.15}[C_2mpyr]_{0.85}[NTf_2]$ and are presented in Figures 10 and 11. The spectra exhibit noticeable differences between the mixed and pure samples. The observed peaks of the $[NTf_2]^-$ anion and $[C_2mpyr]^+$ cation are assigned and summarised in Table S2 based on previous investigations [17, 48-54] The vibrational modes, dominated by the $[NTf_2]^-$ anion, are observed in Raman/IR spectra (278-798 cm^{-1} / 400 -790 cm^{-1}) respectively. The vibrational modes above 880 cm^{-1} are mostly due to the cation $[C_2mpyr]^+$. There is no difference in the IR/Raman spectra of the pure and doped materials in the region 2800 – 3100 cm^{-1} which are attributed to the overtones of methyl and/or alkyl group symmetrical stretching vibrations of the pyrrolidinium cation.

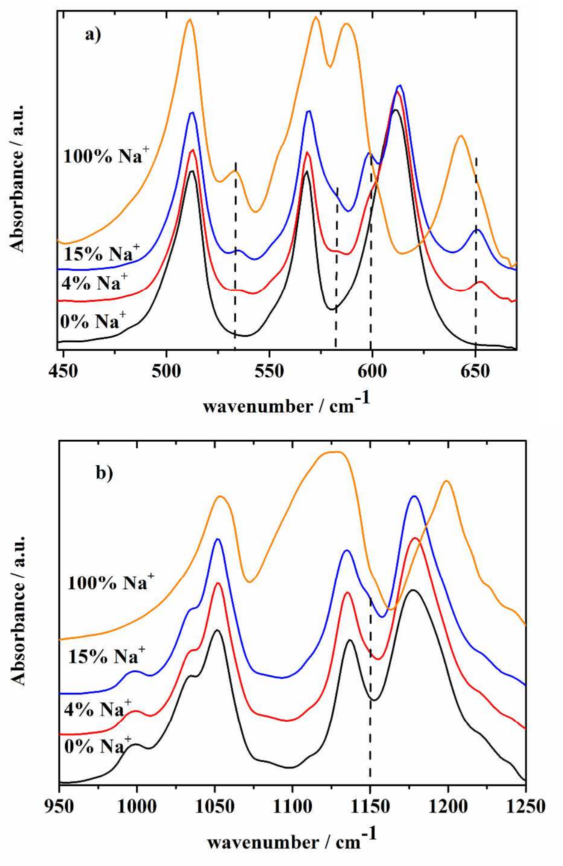

Figure 10. FTIR spectra of pure and mixed materials $NaNTf_2$, $[C_2mpyr][NTf_2]$, $Na_{0.04}[C_2mpyr]_{0.96}[NTf_2]$ and $Na_{0.15}[C_2mpyr]_{0.85}$ NTf_2 at different frequencies a) 450 – 680cm^{-1}, b) 950 – 1250cm^{-1} . Additional weak peaks/shoulders are indicated at ~534, 576, 598, 651 cm^{-1} and 1150 cm^{-1}.

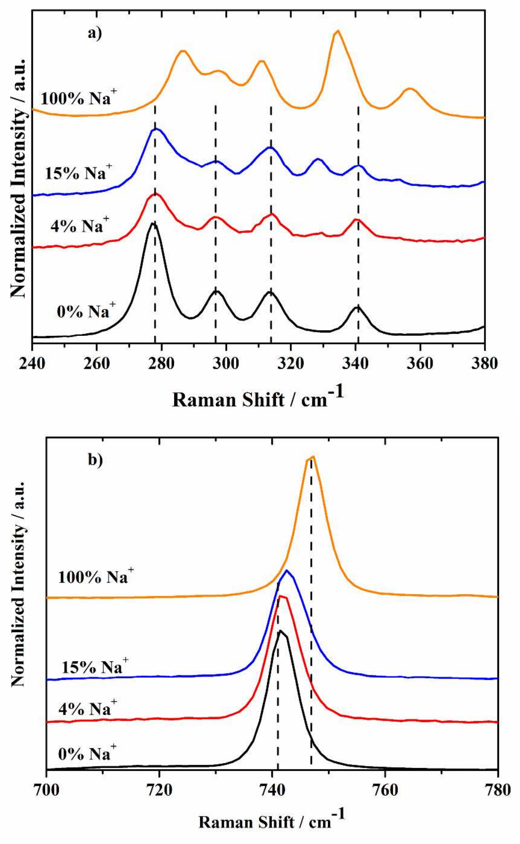

Figure 11. Raman spectra of the pure and mixed materials $NaNTf_2$, $[C_2mpyr][NTf_2]$, $Na_{0.04}[C_2mpyr]_{0.96}[NTf_2]$ and $Na_{0.15}[C_2mpyr]_{0.85}$ NTf_2 at different frequencies (a) 240-380 cm^{-1} and (b) 700-780cm^{-1}. Features (peaks/shoulders) are indicated at ~277, 298, 313 and 341.

The FTIR spectra show several changes with the addition of Na into the OIPC (Figure 10 – changes indicated by vertical dotted lines). There are several new weak peaks and additional shoulders at ~534, 576, 598, 651 and 1150 cm^{-1}, found only in the mixed systems. These may be attributed to interactions with the Na^+ cation leading to changes in the vibrations of the anion, and in particular changes in the SO_2, SNS and CF_3 group vibrations.

The band at 1150 cm^{-1} in this work corresponds to the twisting of the pyrrolidinium rings [54], possibly due to the different chemical environment created by the addition of Na^+, as previously observed in the ^{13}C NMR spectra (Figure 6c) and thus supports a change in ring conformation in the Na rich phase. The characteristic FTIR band for the trans conformer occurs at ~607 cm^{-1}, while the presence of vibration bands at 600 and 653 cm^{-1} indicate the presence of the cis conformer [53]. Previous work by

Lasse`gues et al.[55] indicated the occurrence of a $[Li(NTf_2)_2]^-$ complex which adopted a mixed *C2C1* conformation due to Li interactions with the anion. Herstedt et.al. [56] also found that other vibrations could be indicative of the co-ordination with Li^+, such as the deformation of the SO_2 and CF_3 modes (for example the 571 cm^{-1} IR absorption, involving the deformation of the SO_2 and CF_3 modes exhibit a clear transformation after coordination into a new absorption at 581 cm^{-1}). Our observation of changes in the band positions and also the growth in intensity of new peaks with increasing Na^+ concentration suggests a strong interaction with the NTf_2 anion favouring the cis conformer.

In the Raman spectra (Figure 11) changes occur at 212 cm^{-1}, 300-350 cm^{-1} and 395-415 cm^{-1}. Again the data here support the conclusions from the FTIR spectra indicating the presence of the cis conformer in the mixtures. Martinelli et.al. [52] previously assigned the vibrations at 306, 326, and 333 cm^{-1} to the cis and 298, 314 and 339 for trans conformers in NTf_2. Here we observe Raman bands at 277, 298, 313, 341, 402 and 412 cm^{-1} which are associated to the trans conformer in the pure OIPC, and a new band in the mixed systems at 329 cm^{-1}, slightly red shifted from the $NaNTf_2$ band, corresponding to the cis conformer. Similarly, the 356 cm^{-1} band in the mixed systems has been previously observed for both the trans NTf_2^- and $HMIm^+$ [53]. It was also reported [52] that the intense band at ~740 cm^{-1} can be assigned to two components, a cis conformer at 738 cm^{-1} and trans conformer at 741 cm^{-1}. In the mixed system reported here there is evidence of a broader band at ~740cm^{-1} suggesting the existence of both cis and trans conformers. Thus the vibrational spectroscopy for the mixed systems is consistent with the NMR and XRD data which support the presence of an additional phase. Furthermore it appears that the conformation of the anion in this additional phase is likely to be the cis conformer.

Conclusions

The influence of the addition of $NaNTf_2$ to the OIPC $C_2mpyrNTf_2$ on the phase behaviour and dynamics has been investigated for the first time using DSC, conductivity, SEM, XRD, NMR and vibrational spectroscopy. In contrast to the same OIPC doped with $LiNTf_2$, there is limited solid solution behaviour and a eutectic is readily observed at a composition of about 15mol% $NaNTf_2$ with a eutectic temperature of 63°C, compared to $LiNTf_2$ which showed a eutectic melt at about 25°C at a composition of 33mol% $LiNTf_2$ The conductivity of the $NaNTf_2$/ $C_2mpyrNTf_2$ mixture in lower temperature phases is not enhanced with increasing Na, in contrast to Li system. However, in phase I, well below the eutectic temperature, the ionic conductivity in the solid state increases to reach $3x10^{-4}$S/cm at 60°C for 40 mol% $NaNTf_2$.

Structural characterisation of these Na containing mixtures was undertaken using variable temperature (VT) synchrotron XRD and multinuclear VT solid state NMR. Both measurements show the presence of a second, Na rich phase. The SEM indicates this phase is discretely distributed in the OIPC rich phase even at 2mol% $NaNTf_2$. Whereas the $C_2mpyrNTf_2$ rich phase changes it's crystal system with increasing temperature (from Triclinic P-1 at 273K, to Monoclinic CC at 303K and finally to Orthorhombic 1222 at 328K) the second Na rich phase retains its Monoclinic P2/1 space group. Furthermore, there appears to be little change in the volume in this second phase compared with the OIPC phase. The ^{13}C NMR data and ^{19}F data gave clear evidence of two phases within the material and showed that the pyrrolidinium cation is present in increasing concentration in the second phase. Interestingly both the C_2mpyr cation and the NTf_2^- anion are in significantly different chemical environments in the two phases as seen by the significant chemical shift changes. The additional vibration at $1150cm^{-1}$ in the FTIR also confirms differences in torsion in the pyrrolidinium ring while the new peaks corresponds to the presence of the cis conformation of the NTf_2^- anion in addition to the predominantly trans conformation found in the pure OIPC phase. The ^{23}Na NMR data suggests that the Na ion is found predominantly only in the second phase.

Finally, the ionic conductivity in these systems in the lower temperature phases upon addition of $NaNTf_2$ does not increase in contrast to the corresponding Li containing system. However, in the higher temperature phase, but still below the eutectic temperature, the ionic conductivity in the 15 and 40 mol% sample is significantly higher. The origin of this conductivity is yet to be elucidated although the significant line narrowing in the ^{1}H and ^{19}F NMR data as well as the changes in the ^{23}Na lineshape suggest that all ions are mobile in the higher temperature phase and are thus contributing to the high conductivity. This paper represents the first report of high solid state ionic conductivity in a plastic crystal electrolyte. Interestingly, a second Na rich discrete phase is observed in this system which leads to little effect on the ion mobility in the lower temperature phases, but significant enhancement of ion mobility (as observed from NMR and conductivity) is observed in the higher temperature phases. The work here therefore holds promise that an all solid state Na ion conductor based on OIPCs can be developed, thereby enabling solid state electrochemical devices such as Na batteries.

Acknowledgements

Australian Synchrotron beamtime allocation & SXRD beamline scientists (Dr Justin Kimpton and Dr Helen Brand). All NMR experiments conducted here were undertaken on the NMR facility funded by the ARC LIEF program (grant LE110100141). This work was funded through the ARC Laureate program, MF acknowledges the ARC for her Laureate fellowship.

1. D. R. MacFarlane and M. Forsyth, *Advanced Materials*, 2001, **13**, 957-966.
2. J. N. Sherwood, ed., *The Plastically Crystalline state (Orientally disordered Crystals)*, Wiley-Interscience, 1979.
3. J. Huang, M. Forsyth and D. R. MacFarlane, *Solid State Ionics*, 2000, **136–137**, 447-452.
4. J. Efthimiadis, G. Annat, J. Efthimiadis, D. R. MacFarlane and M. Forsyth, *Solid State Ionics*, 2006, **177**, 95-104.
5. J. Adebahr, F. C. Grozema, S. W. deLeeuw, D. R. MacFarlane and M. Forsyth, *Solid State Ionics*, 2006, **177**, 2845-2850.
6. P. F. Green, in *Kinetics, Transport, and Structure in Hard and Soft Materials*, CRC Press, 2005, pp. 79-122.
7. L. Jin, K. M. Nairn, C. M. Forsyth, A. J. Seeber, D. R. MacFarlane, P. C. Howlett, M. Forsyth and J. M. Pringle, *Journal of the American Chemical Society*, 2012, **134**, 9688-9697.
8. J. M. Pringle, J. Golding, C. M. Forsyth, G. B. Deacon, M. Forsyth and D. R. MacFarlane, *Journal of Materials Chemistry*, 2002, **12**, 3475-3480.
9. J. M. Pringle, P. C. Howlett, D. R. MacFarlane and M. Forsyth, *Journal of Materials Chemistry*, 2010, **20**, 2056-2062.
10. C. M. Forsyth, D. R. MacFarlane, J. J. Golding, J. Huang, J. Sun and M. Forsyth, *Chemistry of Materials*, 2002, **14**, 2103-2108.
11. D. R. MacFarlane, J. Huang and M. Forsyth, *Nature*, 1999, **402**, 792-794.
12. M. Forsyth, J. Huang and D. R. MacFarlane, *Journal of Materials Chemistry*, 2000, **10**, 2259-2265.
13. Y. Abu-Lebdeh, A. Abouimrane, P.-J. Alarco and M. Armand, *Journal of Power Sources*, 2006, **154**, 255-261.

14. J. Efthimiadis, G. J. Annat, J. Efthimiadis, M. Forsyth and D. R. MacFarlane, *Physical Chemistry Chemical Physics*, 2003, **5**, 5558-5564.
15. S. Forsyth, J. Golding, D. R. MacFarlane and M. Forsyth, *Electrochimica Acta*, 2001, **46**, 1753-1757.
16. W. A. Henderson, D. M. Seo, Q. Zhou, P. D. Boyle, J.-H. Shin, H. C. De Long, P. C. Trulove and S. Passerini, *Advanced Energy Materials*, 2012, **2**, 1343-1350.
17. P. C. Howlett, N. Brack, A. F. Hollenkamp, M. Forsyth and D. R. MacFarlane, *Journal of The Electrochemical Society*, 2006, **153**, A595-A606.
18. P. C. Howlett, Y. Shekibi, D. R. MacFarlane and M. Forsyth, *Advanced Engineering Materials*, 2009, **11**, 1044-1048.
19. W. A. a. S. P. Henderson, *Chemistry of Materials*, 2004, **16**, 2881-2885.
20. D. R. MacFarlane, P. Meakin, J. Sun, N. Amini and M. Forsyth, *The Journal of Physical Chemistry B*, 1999, **103**, 4164-4170.
21. J. Adebahr, A. J. Seeber, D. R. MacFarlane and M. Forsyth, *The Journal of Physical Chemistry B*, 2005, **109**, 20087-20092.
22. Y. Shekibi, A. Gray-Weale, D. R. MacFarlane, A. J. Hill and M. Forsyth, *The Journal of Physical Chemistry C*, 2007, **111**, 11463-11468.
23. J. Huang, A. Hill, M. Forsyth, D. MacFarlane and A. Hollenkamp, *Solid State Ionics*, 2006, **177**, 2569-2573.
24. W. A. Henderson, V. G. Young, S. Passerini, P. C. Trulove and H. C. De Long, *Chemistry of Materials*, 2006, **18**, 934-938.
25. W. A. Henderson and S. Passerini, *Chem. Mater.*, 2004, **16**, 2881.
26. L. Jin, P. Howlett, J. Efthimiadis, M. Kar, D. Macfarlane and M. Forsyth, *Journal of Materials Chemistry*, 2011, **21**, 10171-10178.
27. A. J. Hill, J. Huang, J. Efthimiadis, P. Meakin, M. Forsyth and D. R. MacFarlane, *Solid State Ionics*, 2002, **154–155** 119-124.
28. J. Huang, in *School of Chemistry*, Monash Melbourne, 2003.
29. H. Zhu, U. A. Rana, V. Ranganathan, L. Jin, L. O'Dell, D. MacFarlane and M. Forsyth, *Journal of Materials Chemistry A*, 2013.
30. U. A. Rana, P. M. Bayley, R. Vijayaraghavan, P. Howlett, D. R. MacFarlane and M. Forsyth, *Physical Chemistry Chemical Physics*, 2010, **12**, 11291-11298.
31. Y. Yung-Fang Yu and J. T. Kummer, *Journal of Inorganic and Nuclear Chemistry*, 1967, **29**, 2453-2475.
32. J. T. Kummer and N. Weber, 1968.
33. T. Oshima, M. Kajita and A. Okuno, *International Journal of Applied Ceramic Technology*, 2004, **1**, 269-276.
34. D. Wilmer, H. Feldmann and R. E. Lechner, *Physical Chemistry Chemical Physics*, 2002, **4**, 3260-3265.
35. M. Witschas and H. Eckert, *The Journal of Physical Chemistry A*, 1999, **103**, 10764-10775.
36. M. Witschas, H. Eckert, D. Wilmer, R. D. Banhatti, H. Funke, J. Fitter, R. E. Lechner, G. Korus and M. Jansen, *Zeitschrift für Physikalische Chemie*, 2000, **214**, 643.
37. T. Parella, Pulse Program Catalogue: I. 1D & 2D NMR Experiments, http://www.as.miami.edu/chemistry/pdf/NMRmanuals/pulse_program_catalog_1.pdf.
38. B. M. Fung, A. K. Khitrin and K. Ermolaev, *Journal of Magnetic Resonance*, 2000, **142**, 97-101.
39. X. Guan and R. E. Stark, *Solid State Nuclear Magnetic Resonance*, 2010, **38**, 74-76.
40. A. Bielecki and D. P. Burum, *Journal of Magnetic Resonance, Series A*, 1995, **116**, 215-220.
41. D. R. MacFarlane and M. Forsyth, *Adv. Mater.*, 2001, **13**, 957.
42. Y. Shekibi, S. J. Pas, N. M. Rocher, B. R. Clare, A. J. Hill, D. R. MacFarlane and M. Forsyth, *Journal of Materials Chemistry*, 2009, **19**, 1635-1642.

43. Y. Shekibi, J. M. Pringle, J. Sun, S. J. Pas, N. M. Rocher, B. R. Clare, A. J. Hill, D. R. MacFarlane and M. Forsyth, *Journal of Materials Chemistry*, 2010, **20**, 338-344.
44. A. A. Coelho, 2007.
45. S. J. Pas, J. Huang, M. Forsyth, D. R. MacFarlane and A. J. Hill, *The Journal of Chemical Physics*, 2005, **122**, 064704.
46. T. Ungár, *Scripta Materialia*, 2004, **51**, 777-781.
47. P. Wang, Q. Dai, S. M. Zakeeruddin, M. Forsyth, D. R. MacFarlane and M. Grätzel, *Journal of the American Chemical Society*, 2004, **126**, 13590-13591.
48. J. Adebahr, *Electrochimica Acta*, 2003, **48**, 2283-2289.
49. M. Castriota, T. Caruso, R. G. Agostino, E. Cazzanelli, W. A. Henderson and S. Passerini, *The Journal of Physical Chemistry A*, 2004, **109**, 92-96.
50. T. Fujimori, K. Fujii, R. Kanzaki, K. Chiba, H. Yamamoto, Y. Umebayashi and S.-i. Ishiguro, *Journal of Molecular Liquids*, 2007, **131–132**, 216-224.
51. P. Johansson, S. P. Gejji, J. Tegenfeldt and J. Lindgren, *Electrochim. Acta*, 1998, **43**, 1375.
52. A. Martinelli, A. Matic, P. Johansson, P. Jacobsson, L. Börjesson, A. Fernicola, S. Panero, B. Scrosati and H. Ohno, *Journal of Raman Spectroscopy*, 2011, **42**, 522-528.
53. A. M. Moschovi, S. Ntais, V. Dracopoulos and V. Nikolakis, *Vibrational Spectroscopy*, 2012, **63**, 350-359.
54. H. Park, H. S. Kim and Y. M. Jung, *The Journal of Physical Chemistry B*, 2011, **115**, 1743-1750.

55. J.-C. Lasse`gues, J. Grondin, C. Aupetit, and P. Johansson, *J. Phys. Chem. A* **2009,** *113,* 305–314

56. M. Herstedt, M. Smirnov, P. Johansson, M. Chami, J. Grondin, L. Servant and J. C. Lasse` gues *J. Raman Spectrosc.* 2005; **36**: 762–770